AGU PUBLICATIONS

Journal of Advances in Modeling Earth Systems

RESEARCH ARTICLE

10.1002/2015MS000435

Key Points:
- Idealized test cases on a reduced-radius sphere for nonhydrostatic global models
- Good agreement with a Cartesian geometry and analytic solutions
- Demonstrates good accuracy of the numerics in the MPAS dynamic core

Correspondence to:
J. B. Klemp,
klemp@ucar.edu

Citation:
Klemp, J. B., W. C. Skamarock, and S.-H. Park (2015), Idealized global nonhydrostatic atmospheric test cases on a reduced-radius sphere, *J. Adv. Model. Earth Syst.*, *07*, doi:10.1002/2015MS000435.

Received 29 JAN 2015
Accepted 23 JUN 2015
Accepted article online 26 JUN 2015

Idealized global nonhydrostatic atmospheric test cases on a reduced-radius sphere

J. B. Klemp[1], **W. C. Skamarock**[1], **and S.-H. Park**[1]

[1]National Center for Atmospheric Research, Boulder, Colorado, USA

Abstract Idealized simulations on a reduced-radius sphere can provide a useful vehicle for evaluating the behavior of nonhydrostatic processes in nonhydrostatic global atmospheric dynamical cores provided the simulated cases exhibit good agreement with corresponding flows in a Cartesian geometry, and for which there are known solutions. Idealized test cases on a reduced-radius sphere are presented here that focus on both dry and moist dynamics. The dry dynamics cases are variations of mountain-wave simulations designed for the Dynamical Core Model Intercomparison Project (DCMIP), and permit quantitative comparisons with linear analytic mountain-wave solutions in a Cartesian geometry. To evaluate moist dynamics, an idealized supercell thunderstorm is simulated that has strong correspondence to results obtained on a flat plane, and which can be numerically converged by specifying a constant physical diffusion. A simple Kessler-type routine for cloud microphysics is provided that can be readily implemented in atmospheric simulation models. Results for these test cases are evaluated for simulations with the Model for Prediction across scales (MPAS). They confirm close agreement with corresponding simulations in a Cartestian geometry; the mountain-wave results agree well with analytic mountain-wave solutions, and the simulated supercells are consistent with other idealized supercell simulation studies and exhibit convergent behavior.

1. Introduction

Idealized test cases can play a highly beneficial role in evaluating the efficacy of the numerics in atmospheric simulation models. They may allow the model to be applied to highly simplified physical environments that permit the assessment of selective aspects of the model numerics through comparisons with known solutions. In evaluating the numerics in nonhydrostatic global models, however, constructing useful idealized test cases can be problematic. To test the behavior of global models in the nonhydrostatic regime, we face the dilemma that simulations with small grid spacings required to resolve nonhydrostatic phenomena are often beyond the realm of feasibility (and certainly not cost effective). To address this problem, simulations on a reduced-radius sphere have been proposed as a means of achieving nonhydrostatic resolutions at a reasonable computational cost. *Wedi and Smolarkiewicz* [2009] compared the behavior of the Eulerian-Lagrangian modeling system (EULAG) and the Integrated Forecasting System (IFS) dynamical cores through simulations of inertia-gravity waves over idealized terrain on a reduced-radius Earth, and *Ullrich et al.* [2012] proposed several mountain-wave test cases on a reduced-radius sphere for use in the Dynamical Core Model Intercomparison Project (DCMIP), in which a number of modeling groups participated. *Malardel* [2013] has evaluated the treatment of resolved moist deep convection in the IFS using simulations on a reduced-radius Earth.

Of course, atmospheric motions on an Earth sphere of highly reduced radius may have little physical relevance to the real atmosphere, which would negate much of the motivation for pursuing this approach for idealized testing. Therefore, we believe that the most useful test-case configurations are those for which it can be demonstrated that the simulations on the reduced-radius sphere bear strong similarity to physically relevant idealized flow, and for which there are known solutions for comparison. For model testing at nonhydrostatic scales, the relevant physical paradigm is typically flow with or without topography in a Cartesian geometry. By removing Coriolis influences ($f=0$), no rescaling of the natural time or space scales is required since the scale of the disturbances remain small compared to the (infinite) Rossby radius of deformation, regardless of the amount of sphere-radius reduction. Theoretically, solutions on a nonrotating reduced-radius sphere will correspond to those on a Cartesian plane when the disturbances are confined to low latitudes and the depths of disturbances are small compared to the Earth radius (shallow atmosphere approximation). By comparing solutions on the reduced-radius sphere with those obtained in a Cartesian geometry, we can confirm that the solutions on the sphere are not significantly biased by unphysical behavior due to artificial curvature effects.

In this study, we describe idealized test cases on a reduced-radius sphere for both dry dynamics and moist convection, and utilize these cases to evaluate the numerics in our global Model for Prediction Across Scales (MPAS) [*Skamarock et al*., 2012]. We have developed these test cases as part of the High-Impact Weather Prediction Program sponsored by the NOAA Office of Oceanic and Atmospheric Research (OAR) Earth System Research Laboratory (ESRL) for the purpose of facilitating the evaluation of emerging nonhydrostatic global models. These test cases are designed for global models employing the shallow atmosphere approximation (as used in most global models) to reduce the influences of sphere curvature for small sphere-radius simulations.

For the simulation of dry dynamics, we propose two model configurations that are variations from the original DCMIP [*Ullrich et al*., 2012] experiments. These modified cases are flow over a quasi-two-dimensional ridge that can be compared to published results for uniform flow over a two-dimensional ridge [*Schär et al*., 2002; *Klemp et al*., 2003, hereinafter KSF], and flow over a circular mountain that can be compared to 3-D linear analytic solutions for uniform flow over the circular mountain in a Cartesian geometry.

From our experience, simulations of moist convection are often quite revealing since strong latent heating tends to occur near the grid scale (the smallest scales being the most unstable), which is where the model numerics are the most challenged. The simulation of a supercell thunderstorm is well suited for a model test case since these storms are typically characterized by strong isolated long-lived convective cells. Idealized supercell simulations have been conducted since the early days of 3-D convective storm modeling for the purpose of analyzing the dynamics of these powerful storms [*Wilhelmson*, 1974; *Schlesinger*, 1975, 1980; *Weisman and Klemp*, 1982, 1984; *Rotunno and Klemp*, 1982, 1985]. The supercell test case described here is a variation and extension of the idealized supercell case discussed briefly by *Skamarock et al*. [2012], in which a simulation on a flat plane using MPAS with a hexagonal mesh was compared to a corresponding simulation on a rectangular mesh.

2. Mountain-Wave Simulations on the Reduced-Radius Sphere

2.1. Mean Atmospheric Sounding

The intent for these test cases is to simulate the flow of an atmosphere having constant wind and stability over a specified terrain profile on a reduced-radius sphere in the absence of rotation ($\Omega = 0$). Following DCMIP case 2, we initialize the atmosphere with an isothermal mean state at the equator ($T_i(\lambda, 0, z) = T_{eq} = 300$ K) and a zonal wind in solid body rotation with no vertical wind shear such that:

$$u_i(\lambda, \phi, z) = u_{eq} \cos \phi, \tag{1}$$

where $u_{eq} = 20$ m s^{-1}, λ and ϕ designate longitude and latitude, respectively, and the subscript i refers to the initial undisturbed state. The desired balances in the initial state derive from balancing the hydrostatic equation:

$$\frac{\partial \ln p_i}{\partial z} = -\frac{g}{R_d T_i(\phi)}, \tag{2}$$

together with the gradient wind equation:

$$\frac{\partial \ln p_i}{\partial \phi} = -\frac{u_i^2}{R_d T_i(\phi)} \tan \phi = -\frac{u_{eq}^2}{2 R_d T_i(\phi)} \sin 2\phi. \tag{3}$$

Cross differentiating and equating (2) and (3) confirms that in the absence of vertical wind shear, the initial temperature is constant, $T_i(\lambda, \phi, z) = T_{eq}$, and the balanced initial pressure field is given by:

$$p_i(\lambda, \phi, z) = p_{eq} \exp\left(-\frac{u_{eq}^2}{2 R_d T_{eq}} \sin^2\phi - \frac{gz}{R_d T_{eq}}\right), \tag{4}$$

which corresponds to DCMIP (80). As pointed out in the DCMIP test-case document, for a pressure-based vertical coordinate, (4) can be rearranged to provide an equation for the height field (DCMIP equation (84)):

$$z_i(\lambda, \phi, p) = \frac{R_d T_{eq}}{g} \ln\left(\frac{p_{eq}}{p}\right) - \frac{u_{eq}^2 \sin^2\phi}{2g}. \tag{5}$$

2.2. Mountain Topography

For our mountain-wave test cases, we have specified two different terrain profiles, a quasi-two-dimensional ridge that permits comparison with the 2-D test case presented by *Schär et al.* [2002, hereafter referred to as the Schär test case], and a circular mountain terrain as specified in the DCMIP test case 2.1. The Schär test case is interesting as it was designed to evaluate a new treatment for the vertical coordinate (SLEVE coordinate) in the Canadian Mesoscale Compressible Community (MC2) model that removes smaller-scale terrain influences from the coordinate surfaces more rapidly with height than the traditional terrain-following formulation [*Gal-Chen and Sommerville*, 1975]. Using this case, Schär et al. found that distortions in the simulated mountain-wave structure were removed when the traditional terrain-following coordinate was replaced by their proposed SLEVE coordinate. KSF demonstrated that the fundamental source of error in this test case arises when there is an inconsistency in the numerical representation of the metric terms that appear in the dynamical equations that employ a terrain-following vertical coordinate. This is an informative test case in that there is a linear analytic solution for comparison and a clear understanding of the aspects of the numerics to which model results are most sensitive.

The general form of the terrain profile for both of our mountain-wave test cases follows the formulation specified for DCMIP case 2.1:

$$z_s(\lambda,\phi)=h_0\exp\left[-\frac{r(\lambda,\phi)^2}{d_0^2}\right]\cos^2\left[\frac{\pi r(\lambda,\phi)}{\xi_0}\right], \tag{6}$$

(DCMIP, equation (76)). For the circular mountain profile used in DCMIP 2.1, $r(\lambda,\phi)$ is the great-circle distance from the mountain center at (λ_c,ϕ_c), as defined in DCMIP (77):

$$r(\lambda,\phi)=\frac{a_{ref}}{X}\arccos\left[\sin\phi_c\sin\phi+\cos\phi_c cos\phi\cos(\lambda-\lambda_c)\right], \tag{7}$$

where a_{ref} is the full Earth radius, X is the reduced Earth-radius scaling factor, $h_0=250$ m, $d_0=5000$ m, and $\xi_0=4000$ m. The terrain defined by (6) and (7) was configured such that the profile along its centerline (equator) is identical to the 2-D terrain used in the Schär test case.

To achieve similarity with the 2-D Schär case, we have modified the circular mountain profile (6) by retaining the terrain shape along the equator, and then extending this longitudinal terrain profile to form a ridge in the north-south (latitudinal) direction, with the height and width gradually reduced to zero approaching the poles (i.e., multiplying the 2-D terrain profile by $\cos\phi$). In this manner, the mountain-wave structure along the equator should be very similar to the 2-D solutions published by *Schär et al.* [2002] and KSF. For this purpose, we alter the terrain specified in (6) and (7) by defining the distance $r(\lambda,\phi)$ used in (6) as the distance along the Earth's surface from the ridge axis (at $\lambda=\lambda_c$) in the longitudinal direction. With this modification, the expression for $r(\lambda,\phi)$ becomes

$$r(\lambda,\phi)=\frac{a_{ref}}{X}(\lambda-\lambda_c)\cos\phi=r_0(\lambda)\cos\phi, \tag{8}$$

In (6), the maximum ridge height along its centerline is $z_i(\lambda_c,\phi)=h_0\cos\phi$, such that $Nz_s(\lambda_c,\phi)/u_i(\phi)$, a measure of the nonlinearity of the flow, remains independent of ϕ. Similarly, the horizontal length scales of the terrain ($d=d_0\cos\phi,\ \xi=\xi_0\cos\phi$) are scaled with latitude so that the ratio of the vertical length scale (u_i/N) to the horizontal scale also does not depend on latitude. The expression for the terrain height then becomes

$$z_s(\lambda,\phi)=h_0\exp\left[-\frac{r_0(\lambda)^2}{d_0^2}\right]\cos^2\left[\frac{\pi r_0(\lambda)}{\xi_0}\right]\cos(\phi). \tag{9}$$

2.3. Model Configuration for the Quasi Two-Dimensional Mountain Ridge Case

Here the intent is to define a model configuration that will provide good quantitative agreement with the 2-D test case investigated by *Schär et al.* [2002] and KSF. For this purpose, we specify a reduced-radius scaling factor of $X=166.7$, which is one-third the scaling factor of $X=500$ used for DCMIP 2.1. This larger radius sphere is adopted to minimize the effects of sphere curvature, and to prevent the mountain-wave disturbances from circling the globe during a 2 h simulation. Maintaining similarity with the Schär test case, we specify the model top $z_{top}=20$ km, with an absorbing layer employed above $z_h=10$ km. We configure the absorbing

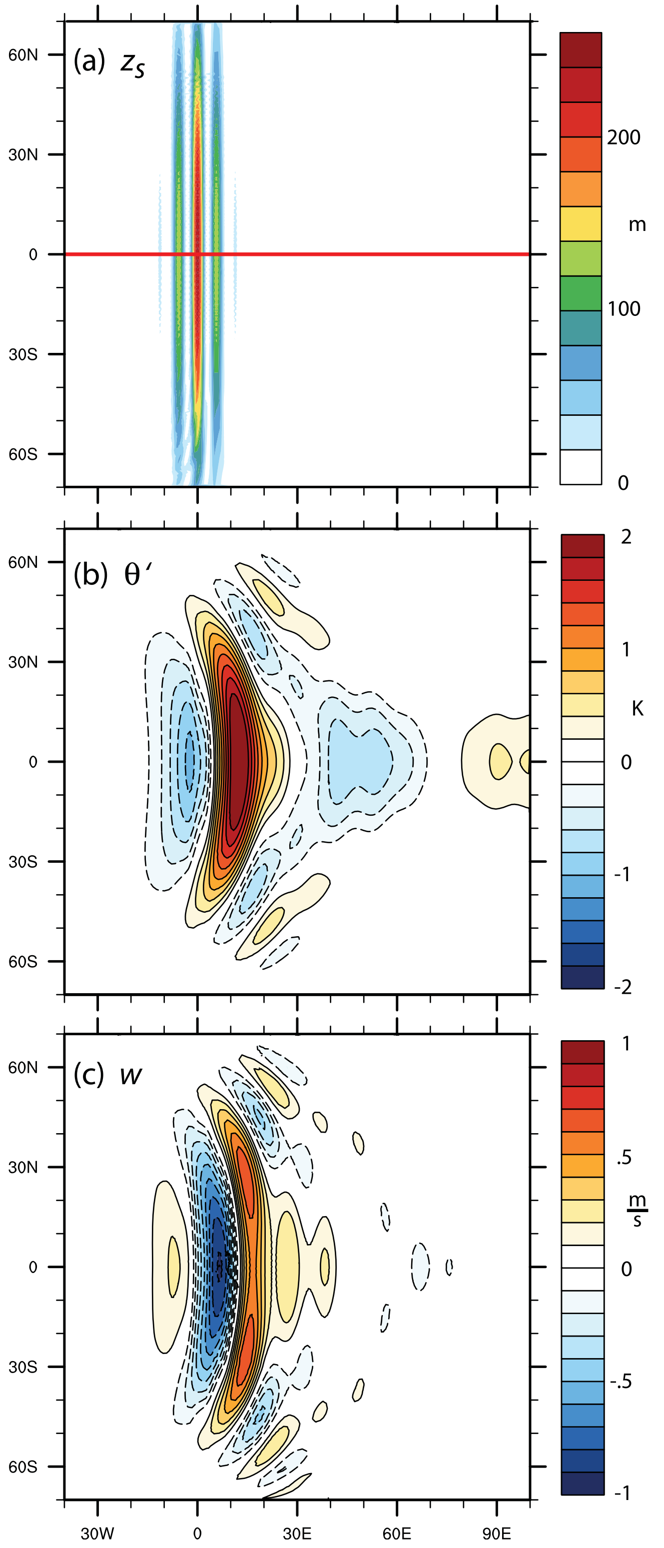

Figure 1. (a) Ridge-like terrain profile z_s as represented in (9) for $h_0=250$ m. Horizontal cross sections from an MPAS simulation with $h_0=250$ m at 8 km at 2 h for (b) perturbation potential temperature θ' and (c) vertical velocity w.

layer through implicit *Rayleigh* damping of vertical velocity [*Klemp et al.*, 2008]. (The absorbing layer can also be specified using explicit *Rayleigh* damping as proposed in DCMIP (78) and (79), if preferred.) For the ridge terrain profile, we find that a horizontal grid spacing of about 1.1° (∼720 m), and a vertical grid spacing of ∼ 500 m is sufficient to accurately capture the wave development of interest above the mountain (to 10 km) and provide good semiquantitative agreement with the linear analytic solution for the 2-D case. For the MPAS centroidal Voronoi grid, this horizontal cell spacing is achieved using the 40,962 cell uniform mesh (nominally hexagons). The transport terms are computed using a third-order scheme with reduced dissipation ($\beta=0.25$), as described in *Skamarock and Gassmann* [2011], and no additional explicit dissipation is included. The time step used for the model integration is $\Delta t=12$ s.

2.4. MPAS Results for the Quasi Two-Dimensional Mountain Ridge Case

The ridge terrain profile for $h_0=250$ m is depicted in Figure 1a. Although in this map projection the horizontal scale of the terrain appears to be independent of latitude, the physical horizontal scale is decreasing in proportion to cos ϕ as discussed above. Horizontal cross sections of the perturbation potential temperature θ' and vertical velocity w at 8 km are displayed in Figures 1b and 1c, respectively. The wave structure over the central portion of the ridge is reasonably two dimensional, with more noticeable three-dimensional structure appearing at higher latitudes, where both the terrain height and wind speed have decreased significantly from their amplitudes along the equator.

To compare results with the 2-D wave structure discussed by Schär and KSF, we display in Figure 2a the vertical cross section of the vertical velocity along the ridge centerline (equator) for the terrain profile as defined in (9), but with a maximum height $h_0=25$ m to ensure that the wave response is essentially linear. Following KSF, we have also derived the linear analytic solution for the corresponding flow

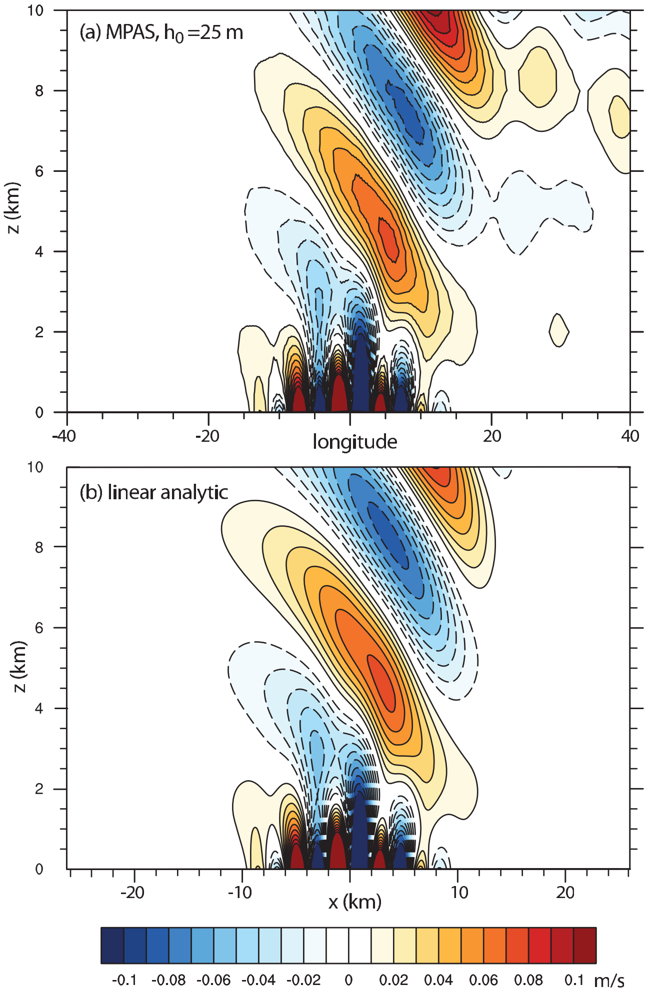

Figure 2. (a) West-east vertical cross section of vertical velocity along the ridge centerline from an MPAS simulation using a linear mountain height $h_0=25$ m at 2 h. (b) Vertical cross section of vertical velocity from the 2-D linear analytic solution for $h_0=25$ m.

over a 2-D ridge, which is shown in Figure 2b. For reference, we have included the derivation of this linear solution in Appendix A. This wave structure arises due to the combination of shorter-scale evanescent waves at low levels forced by the narrow ridges, together with the longer wavelength modes aloft forced by the broader terrain envelope. The good semiquantitative agreement of the MPAS simulation with the 2-D analytic solution confirms that the grid structure is sufficient to resolve the dominant wave response, and that the specified ridge profile and the Earth-radius reduction allow a reasonable correspondence with the 2-D behavior on a flat plane. The trailing perturbations evident at higher levels in Figure 2a, however, reflect the residual 3-D influences due to spherical effects on the reduced-radius Earth.

Figure 3 displays the vertical cross sections for w along the ridge centerline at 2 h for a maximum terrain height $h_0=250$ m, as used by *Schär et al*. [2002] and KSF. These fields are quite similar to the 2-D simulations in those papers and to the 2-D results obtained previously with MPAS [*Skamarock et al*., 2012]. (Notice that vertical velocity perturbations shown here are a factor of two greater than those in these previous papers since the mean wind and stability are twice as large for this isothermal environment.) The amplitudes of the waves are slightly more than a factor of 10 stronger than those shown in Figure 2 for $h_0=25$ m, due to the presence of weak nonlinear effects. These panels illustrate the importance of using consistent numerics in representing the metrics in the terrain-following coordinate transformation (shown for a height-based terrain-following coordinate as used in MPAS). As discussed by KSF, this issue is most critical for the treatment of the coordinate metric ζ_x that appears in the expression for $\omega=u\zeta_x+w\zeta_z$. Figure 3 documents that using either fourth-order (Figure 3a) or second-order (Figure 3b) numerics for the horizontal advection terms yields accurate results provided the coordinate metric ζ_x is computed using the same order numerics. In contrast, using fourth-order advection together with second-order numerics for the metric term leads to spurious perturbations (Figure 3c), as documented by KSF.

2.5. Model Configuration for the Circular Mountain Case

The circular mountain case using (6) and (7) is similar to DCMIP case 2.1, except that we again specify a smaller sphere-radius reduction $X=166.7$ to reduce curvature effects and prevent disturbances from circling the globe during a 2 h integration. For this case, we have raised the model top to $z_{top}=30$ km (with a damping layer above 20 km) to capture more of the nonhydrostatic wave train that extends downstream from the mountain. We note, however, that this greater domain depth begins to cause discrepancies from the corresponding wave structure in a Cartesian geometry due to the increasing influences of spherical

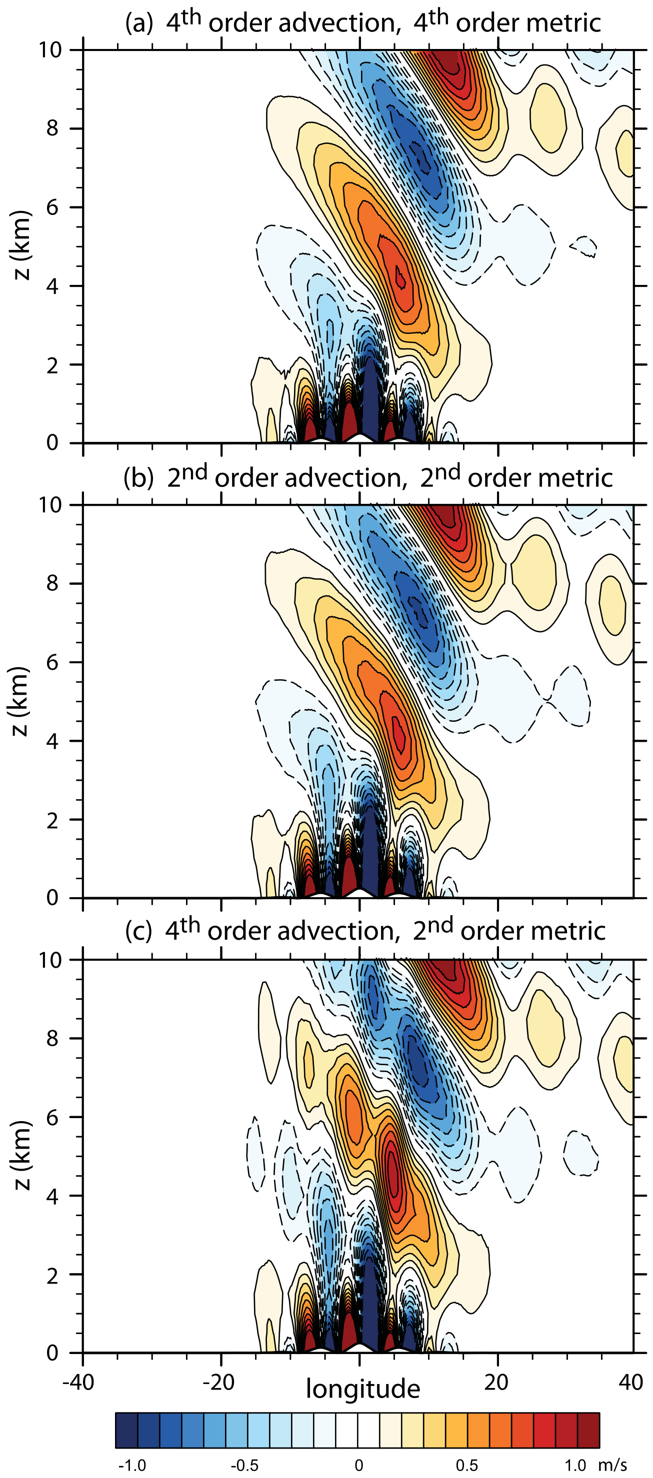

Figure 3. West-east vertical cross sections of vertical velocity along the ridge centerline from MPAS simulations for $h_0=250$ m at 2 h. (a) Fourth-order horizontal advection with fourth-order terrain-following metric terms; (b) second-order horizontal advection with second-order terrain-following metric terms; and (c) fourth-order horizontal advection with second-order terrain-following metric terms.

effects. Because of the more significant smaller-scale structure in the nonhydrostatic wave train produced by the circular mountain, we have specified a smaller horizontal grid spacing of ~360 m (one-half that used for the ridge mountain simulations). We have specified a nominal vertical grid spacing of 250 m to resolve the smaller-scale vertical structure in this case, and integrate over time using $\Delta t=6$ s. (A vertical grid spacing of 500 m was found to be less accurate in comparisons with the linear analytic solution.)

2.6. MPAS Results for the Circular Mountain Case

Figure 4 illustrates the evolution of potential temperature and vertical velocity over the circular mountain defined by (6) and (7) for $h_0=250$ m. The mountain waves developing in response to the uniform flow over this terrain exhibit a strong nonhydrostatic wave train that extends downstream of the mountain as well as laterally. The somewhat noisy fields at the downstream edge of the expanding wave train are the remnants of the startup vortex arising from the impulsive insertion of the terrain at the beginning of the integration.

Figure 5 provides a comparison of the vertical θ and w cross sections at 2 h for the simulation on the reduced-radius sphere with corresponding behavior in a Cartesian geometry. To produce the Cartesian-geometry solution, we have reconfigured the MPAS grid to represent a flat plane of hexagonal grid cells with doubly periodic lateral boundaries. In addition, we have derived the 3-D linear steady state analytic solution for uniform flow over the circular mountain in a Cartesian geometry (see derivation in Appendix B). In these vertical cross sections, the MPAS simulation in the Cartesian geometry exhibits good agreement with the linear analytic solution, confirming that the grid resolution is sufficient to accurately capture the nonhydrostatic wave structure. The small discrepancies in the simulated results are likely due to weak nonlinear effects and slight departures from steady state. In the simulation on the sphere, the vertical velocity field at 2 h is quite similar to the results in a Cartesian geometry. However, the potential temperature perturbations are more strongly

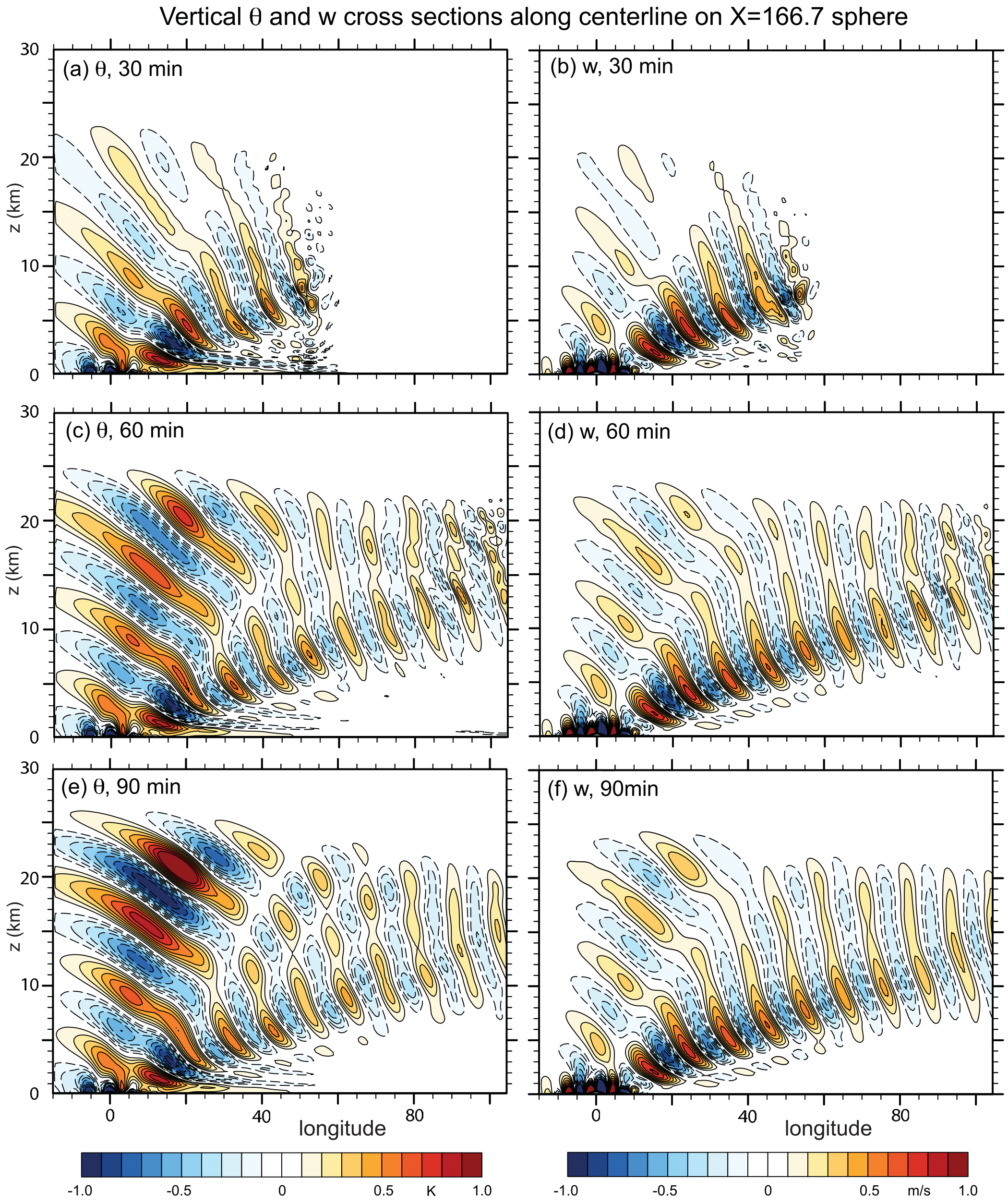

Figure 4. Vertical cross sections for θ' and w in the streamwise direction along the mountain centerline on the reduced-radius sphere with $X = 166.7$ at t = 30, 60, and 90 min.

affected by spherical influences, and begin to exhibit significant departures from those in the Cartesian geometry at upper levels, as evidenced by the smaller vertical scales appearing in the potential temperature field downstream of the mountain at altitudes between 10 and 20 km.

The comparison with numerical and analytic solutions in a Cartesian geometry is further illustrated in horizontal cross sections for these variables. Figure 6 depicts these cross sections at 2 h at a height of 8 km for the simulations on the sphere and flat plane, as well as the linear analytic solution. At this altitude, there is good agreement between the solutions on the sphere and the flat plane. Notice, however, that the potential temperature perturbations extend further in latitude than those for vertical velocity and show some departure from the Cartesian behavior at the higher latitudes. Figure 7 shows these same fields at 2 h at a height of 16 km. Since the wave train expands laterally as well as downstream as the wave energy propagates upward from the circular mountain, at this higher altitude, the waves have greater amplitude at higher latitudes. Notice, for example, that the vertical velocity perturbations at 8 km (Figure 6b) have little

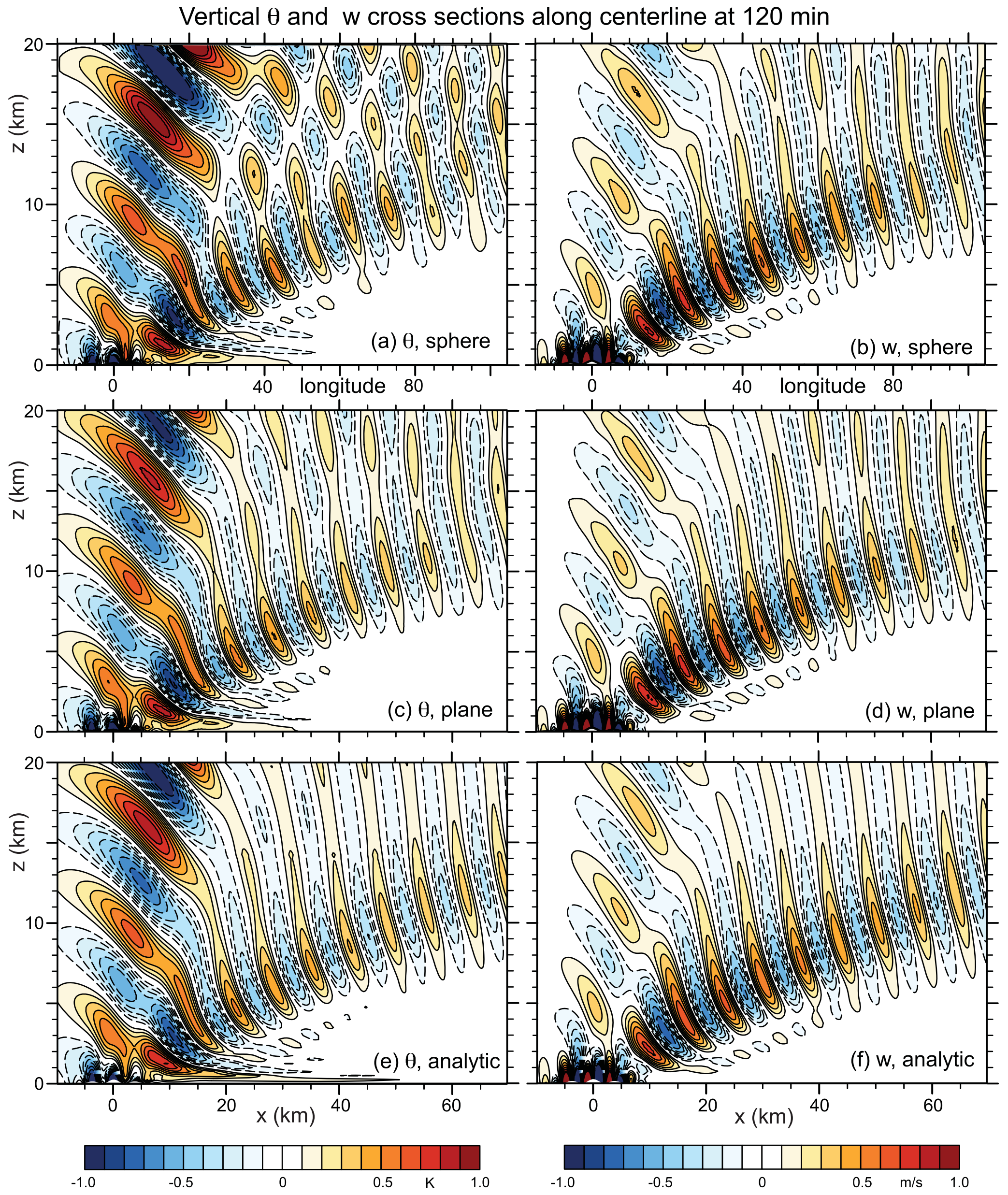

Figure 5. Vertical cross sections for θ' and w in the streamwise direction along the mountain centerline at t = 120 min for the (a and b) reduced-radius sphere and (c and d) flat plane. (e and f) The corresponding 3-D linear analytic solution from Appendix B.

amplitude poleward of about ±25° latitude, while at 16 km (Figure 7b) there are noticeable perturbations in the 30°–60° latitude range that depart from the vertical velocity field obtained on the flat plane (Figure 7d). Even greater departures are apparent in the potential temperature perturbations at this height. Thus, for the model configuration used for this test case, good quantitative agreement with mountain waves in a Cartesian geometry should only be expected below about 10 km in altitude.

For this case, the mountain waves exhibit a strong nonhydrostatic character, with significant propagation of wave energy downstream as well as in the vertical. Nevertheless, including an absorbing layer to prevent artificial reflections of wave energy from the model top is essential to obtaining accurate solutions. The impact of the upper absorbing layer is evident in comparison with the corresponding solution obtained with the absorbing layer removed, shown in Figure 8, which depicts the respective vertical cross sections for the potential temperature and vertical velocity along the equator at 2 h. These results emphasize the importance of absorbing the upward propagating gravity-wave energy to prevent significant artificial reflection from the upper

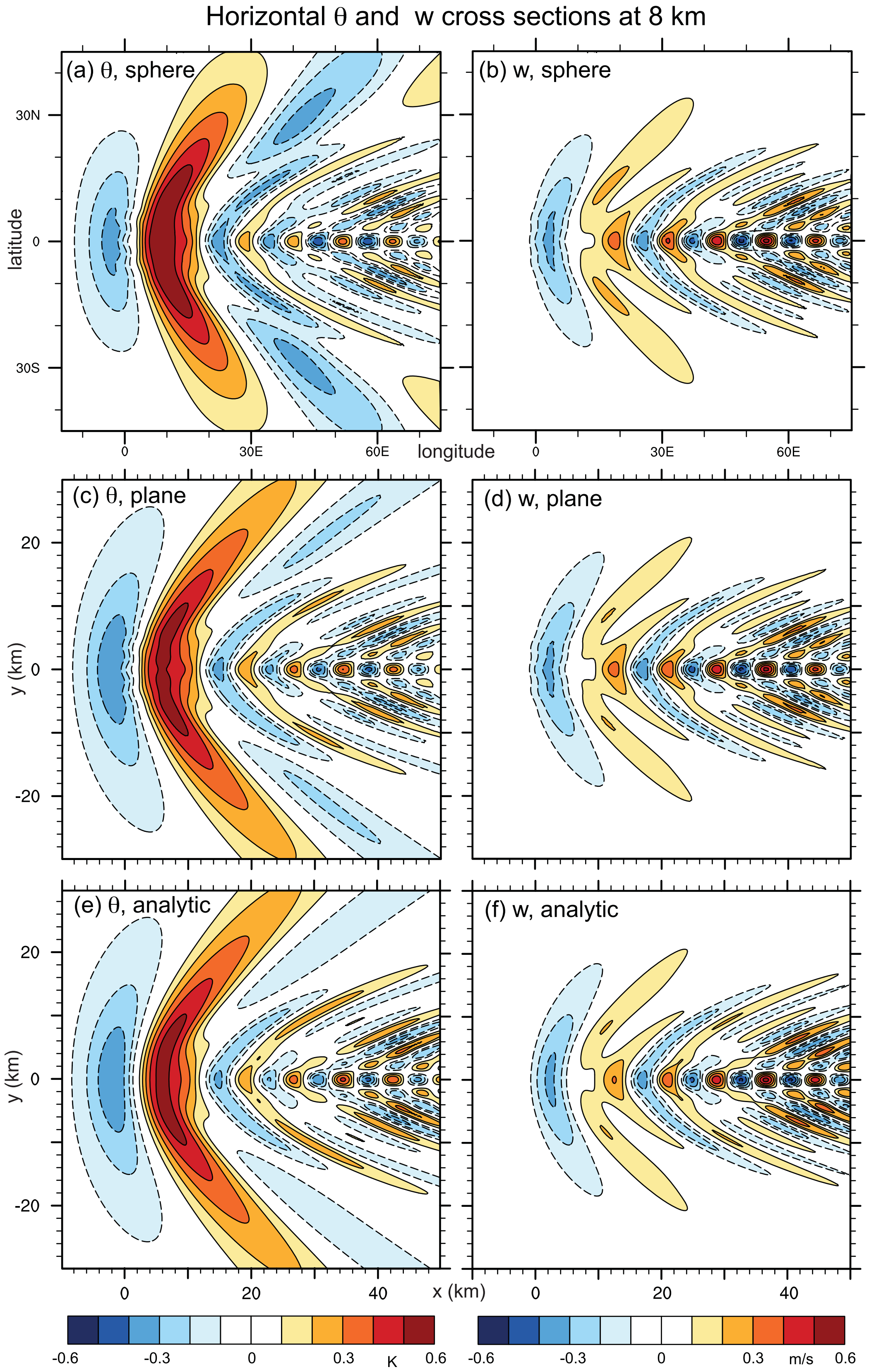

Figure 6. Horizontal cross sections for θ' and w at $z = 8$ km at t = 120 min for the (a and b) reduced-radius sphere and (c and d) flat plane. (e and f) The corresponding linear analytic solution from Appendix B.

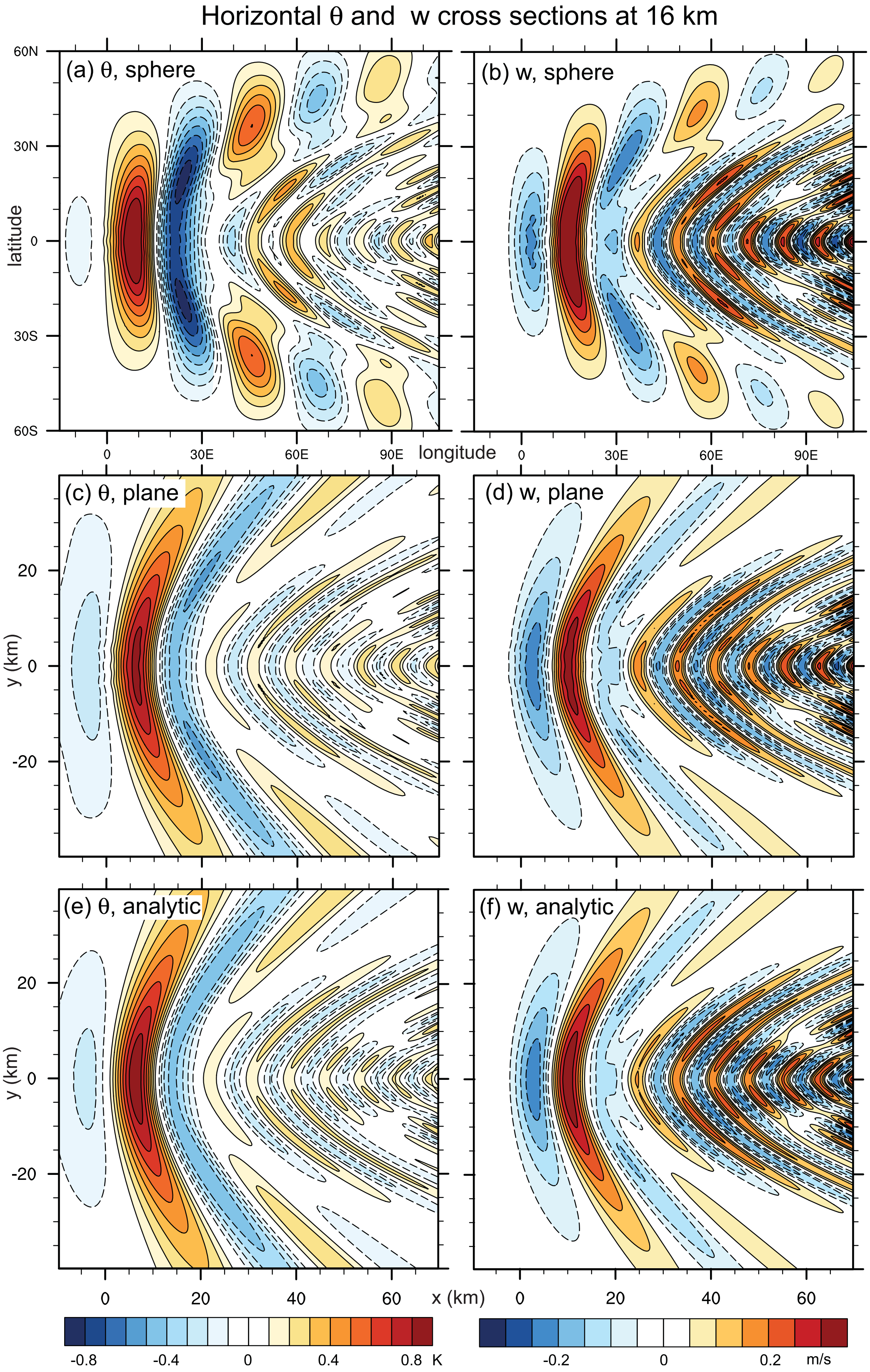

Figure 7. Horizontal cross sections as in Figure 6, except at $z = 16$ km.

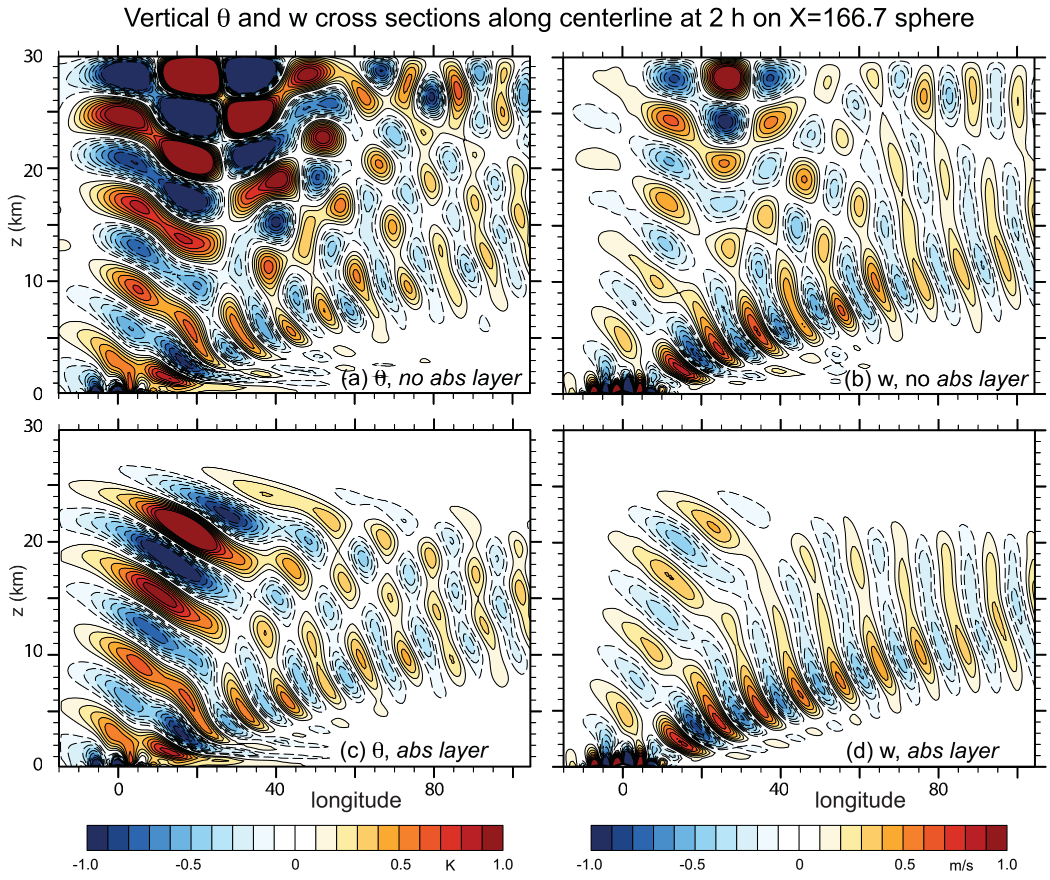

Figure 8. Vertical cross sections for θ' and w in the streamwise direction along the mountain centerline on the reduced-radius sphere with X = 166.7 at t = 2 h (a and b) with no upper absorbing layer and (c and d) with an absorbing layer in the region z = 20–30 km.

boundary of the domain. Without an absorbing layer, model solutions for this case will exhibit strong distortions due to wave reflection unless the model numerics themselves are highly dissipative.

3. Supercell Simulations on the Reduced-Radius Sphere

Supercell thunderstorms are typically characterized by strong, long-lived convective cells containing deep, persistent rotating updrafts. Because of their rotational characteristics, they may propagate transverse to the prevailing winds and may split into two counterrotating storms [*Rotunno and Klemp*, 1982, 1985].They often produce heavy precipitation, large hail, damaging surface winds, and produce most of the world's intense tornadoes. Because of their large characteristic scales (O(10 km) wide updrafts) and long (several hour) persistence, nonhydrostatic global models should be expected to explicitly simulate these supercell storms as these models approach O(km) grid spacings.

As mentioned above, simulating moist convection in a conditionally unstable environment can provide a challenging test for the model numerics. Since the smallest horizontal scales tend to be the most unstable in a conditionally unstable atmosphere [*Rayleigh*, 1916], latent heating can infuse significant energy near the grid scale, which is where the accuracy and stability of the numerics are most crucial.

The explicit treatment of moist convection requires the inclusion of cloud microphysics to represent the condensation and evaporation of water species, as well as precipitation processes. For this purpose, we adopt a simple warm-rain Kessler-type microphysics that is encapsulated in a single small subroutine (about 40 executable lines of code, see Appendix C) that can be readily implemented in any nonhydrostatic model.

Dissipation is also an important process in simulating moist convection. Although the smallest scales tend to be the most unstable, dissipation processes are also strongest at the smallest scales. Therefore, the dominant scales that arise in moist unstable convection are strongly regulated by the relative strengths of latent heating and dissipation at these smaller scales [*Rayleigh*, 1916] (as described by *Ching et al*. [2014]). For a test case, we believe it is important that the solution can be converged, at least in principle, as the finite difference increments are reduced. This requires that the physical dissipation be independent of the model grid size, which is not the case in most subgrid turbulence parameterizations. Thus, we employ a constant coefficient second-order diffusion for these supercell simulations. For explicit moist convective simulations, the dissipative processes should be considered part of the model physics, and not just a numerical filter to maintain stability.

3.1. Mean Atmospheric Sounding

For this supercell test case, we initialize the atmosphere with an idealized thermodynamic sounding that has large CAPE ($\sim$2200 m^2 s^{-2}) and strong low-level wind shear, which together are conducive for supercell formation. Following *Weisman and Klemp* [1982, 1984] and *Weisman et al*. [1988], we specify the mean potential temperature profile at the equator $\bar{\theta}_{eq}(z)$ as

$$\bar{\theta}_{eq}(z)=\begin{cases} \theta_0+(\theta_{tr}-\theta_0)\left(\frac{z}{z_{tr}}\right)^{\frac{5}{4}}, & \text{for } z \le z_{tr}\,; \\ \theta_{tr}\exp\left[\dfrac{g}{c_p T_{tr}}(z-z_{tr})\right], & \text{for } z > z_{tr}\,, \end{cases} \tag{10}$$

where $\theta_0=300$ K is the surface potential temperature, and $\theta_{tr}=343$ K represents the potential temperature at the tropopause at $z_{tr}=12$ km. The stratosphere is isothermal at $T_{tr}=213$ K. The relative humidity profile $H(z)$ is given by

$$H(z)=\begin{cases} 1-\dfrac{3}{4}\left(\dfrac{z}{z_{tr}}\right)^{\frac{5}{4}}, & \text{for } z \le z_{tr}\,; \\ \dfrac{1}{4}, & \text{for } z > z_{tr}\,. \end{cases} \tag{11}$$

The initial water-vapor mixing ratio is defined from $\bar{q}_v(z)=H(z)\bar{q}_{vs}$, where the saturation mixing ratio is taken from *Klemp and Wilhelmson* [1978, equation (2.11)]:

$$\bar{q}_{vs}(z)=\frac{380}{\bar{p}_{eq}(z)}\exp\left(17.27\,\frac{T_{eq}(z)-273}{T_{eq}(z)-36}\right). \tag{12}$$

Here the initial pressure at the equator $\bar{p}_{eq}(z)$ is expressed in hPa, and $T_{eq}(z)$ is the initial unperturbed temperature at the equator. In addition, the mixing ratio is constrained to a maximum value of $q_{v0}=14$ g/kg to approximate a well-mixed boundary layer in the lowest kilometer. The temperature and moisture profiles for this sounding are shown in Figure 9.

In past idealized supercell simulations, we have used an environmental wind profile characterized by either a hyperbolic tangent function [*Weisman and Klemp*, 1982], or a linear shear below $z_s=5$ km, with constant winds aloft [*Weisman and Klemp*, 1986; *Weisman et al*., 1988]. We have chosen the latter wind profile for this test case as we found that it produced a somewhat steadier mature supercell. However, in balancing the initial state on the sphere as discussed below, a discontinuity in the mean wind shear ($\partial\bar{u}/\partial z$) leads to a discontinuity in potential temperature away from the equator. Therefore, we have removed this discontinuity by specifying a polynomial fit for $\bar{u}$ for $z_s-1000 < z < z_s+1000$ that matches the value and slope of $\bar{u}$ at $z=z_s\pm1000$. The mean wind is then scaled by $\cos\phi$ to maintain solid-body rotation at each level on the sphere, yielding:

$$\bar{u}(\phi,z)=\begin{cases} \left[U_s\left(\dfrac{z}{z_s}\right)-U_c\right]\cos\phi & \text{for } z < z_s-1000\,; \\ \left[\left(-\dfrac{4}{5}+3\dfrac{z}{z_s}-\dfrac{5}{4}\dfrac{z^2}{z_s^2}\right)U_s-U_c\right]\cos\phi & \text{for } |z-z_s| < 1000\,; \\ [U_s-U_c]\cos\phi & \text{for } z > z_s+1000\,. \end{cases} \tag{13}$$

We specify $U_s=30$ m s^{-1} to provide a strong wind shear that is a typical strength for supercell storm environments, and set a coordinate translation speed $U_c=15$ m s^{-1} at the equator to render the storm nearly stationary in the model coordinates. Defining $U_{eq}=\bar{u}(0,z)$, the ground relative initial wind at the equator is then $\bar{u}_{eq}(z)+U_c$ (see Figure 9).

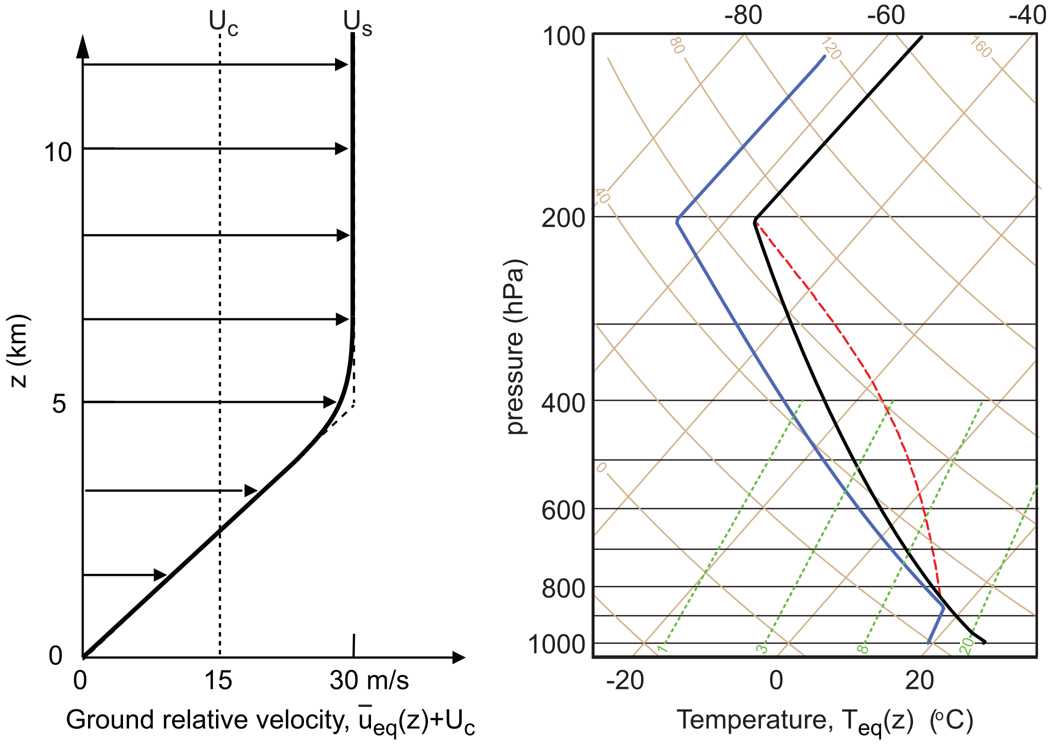

Figure 9. Mean wind and thermodynamic sounding at the equator for the supercell simulation on a reduced-radius sphere. The skew-T plot displays the temperature (black line), dew point (blue line), and the moist adiabat for surface parcel ascent (dashed red line).

Although there is no Coriolis force in these simulations, the presence of vertical wind shear requires latitudinal variation of both the potential temperature and pressure to maintain a balanced state in the absence of imposed perturbations. As in the mountain-wave test case, the initial fields must satisfy both the hydrostatic equation:

$$\frac{\partial \bar{\pi}}{\partial z} = -\frac{g}{c_p \bar{\theta}_v}, \tag{14}$$

and the gradient wind equation:

$$\bar{u}^2 \tan\phi = -c_p \bar{\theta}_v \frac{\partial \bar{\pi}}{\partial \phi}, \tag{15}$$

where $\bar{\theta}_v$ is the virtual potential temperature and $\bar{\pi}$ is the Exner function. (Equations (14) and (15) are the same as (2) and (3), except written in terms of (π, θ_v) instead of (p, T).) Cross differentiating these two equations and equating $\bar{\pi}_{\phi z}$, we obtain the following equation for $\bar{\theta}_v$:

$$\frac{\partial \bar{\theta}_v^{(i+1)}}{\partial \phi} = \frac{\sin 2\phi}{2g} \left\{ U_{eq}^2 \frac{\partial \bar{\theta}_v^{(i)}}{\partial z} - \bar{\theta}_v^{(i)} \frac{\partial U_{eq}^2}{\partial z} \right\}, \tag{16}$$

This equation can be readily solved by iteration (as indicated by the *i* superscripts), and is found to converge in two to three iterations. After computing a balanced $\bar{\theta}_v$ from (16), the corresponding balanced pressure is obtained from the hydrostatic equation (14), after adjusting the pressure along the top of the domain using (15). The moisture $\bar{q}_v(z)$ is computed based on the thermodynamic sounding at the equator, and does not vary with latitude. The variations of the balanced initial thermodynamic fields with latitude are displayed in Figure 10. The maximum deviations (about 2.5° K for θ and -1 mb for p) occur at the surface at the poles. Notice that these variations from their values at the equator depend only on latitude, and not on the radius reduction of the sphere.

3.2. Model Configuration for the Supercell Case

For this supercell test case on a reduced-radius sphere, we specify a radius reduction factor of $X = 120$, which provides a large enough sphere to maintain good quantitative correspondence with comparable

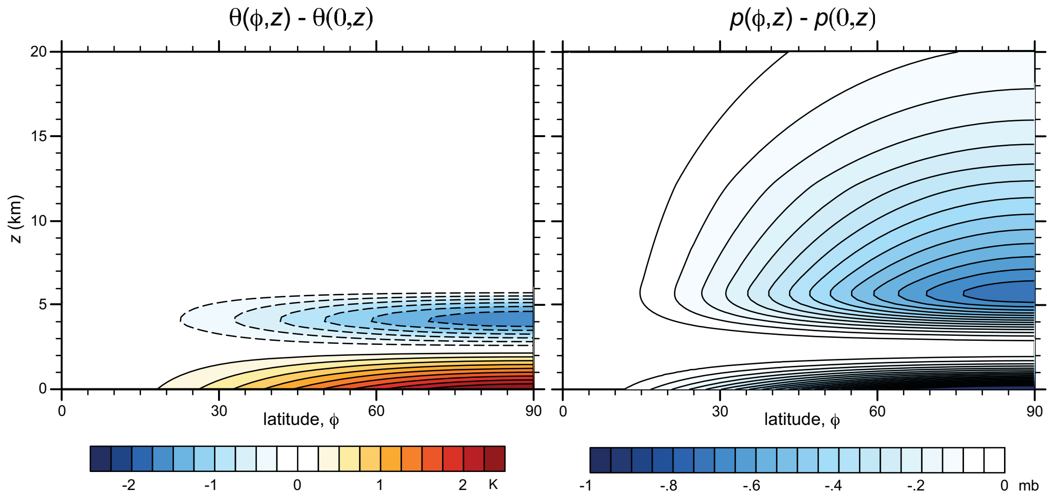

Figure 10. Deviation of potential temperature (K) and pressure (hPa) from their values at the equator as a function of latitude.

simulations on a flat plane (see further discussion in the results section). The simulation domain is 20 km in depth, with a uniform vertical grid spacing of $\Delta z = 500$ m and a free-slip boundary condition is imposed along the lower surface. We begin with a nominally uniform horizontal grid spacing of about 500 m (~0.5° mesh, containing 163,842 grid cells), which appears to yield nearly converged solutions with the diffusion specified as outlined below. Coarser horizontal grids will also be considered to evaluate the dependence of simulated storm evolution as a function of horizontal resolution. The transport terms are computed with third-order numeric [*Skamarock and Gassmann*, 2011] without reduced dissipation ($\beta = 1.0$), and for simplicity, neither the positive-definite nor monotonic options are active. With the 500 m grid, we integrate MPAS forward in time using a 3 s time step, while for coarser grids, the time step is increased proportionately.

3.3. Initial Thermal Perturbation

To initiate convection, a thermal perturbation is introduced in the initial potential temperature field. It is defined according to the expression

$$\theta_i(\lambda,\phi,z) = \begin{cases} \bar{\theta}(\phi,z) + \Delta\theta \cos^2\left(\frac{\pi}{2}R_\theta\right) & \text{for } R_\theta < 1\,; \\ \bar{\theta}(\phi,z) & \text{for } R_\theta \geq 1\,, \end{cases} \tag{17}$$

where

$$R_\theta = \left[\left(\frac{r}{r_h}\right)^2 + \left(\frac{z - z_c}{r_z}\right)^2\right]^{\frac{1}{2}}. \tag{18}$$

Here $r(\lambda,\phi)$ is the great-circle distance from the center of the thermal perturbation at (λ_c,ϕ_c) as defined by (6). The parameters in (17) and (18) are specified as $\Delta\theta = 3$ K, $r_h = 10$ km, and $z_c = r_z = 1.5$ km.

3.4. Cloud Microphysics

To represent the cloud microphysical processes, we utilize a simple Kessler-type parameterization [*Kessler*, 1969] that contains three moisture species: water vapor (q_v), cloud water (q_c), and rainwater (q_r). This parameterization follows the implementation by *Soong and Ogura* [1973] as described in *Klemp and Wilhelmson* [1978]. The microphysics subroutine (see Appendix C) is called at the end of each time step and updates the potential temperature and moisture variables according to the equations:

$$\frac{\Delta\theta}{\Delta t} = -\frac{L}{c_p \pi}\left(\frac{\Delta q_{vs}}{\Delta t} + E_r\right), \tag{19}$$

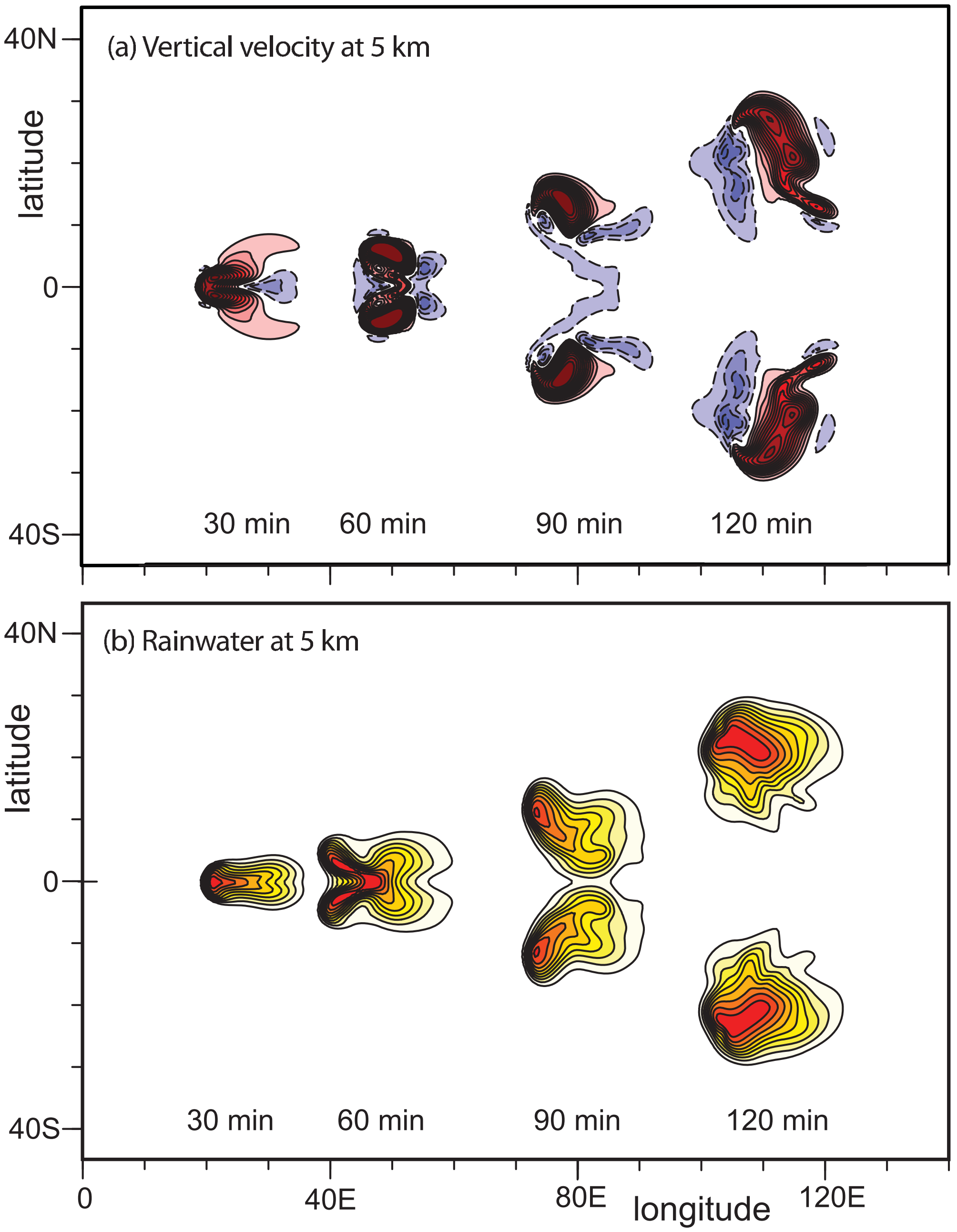

Figure 11. Horizontal cross sections for the simulation with $X=120$ and $\Delta\sim 500$ m at 5 km at 30 min intervals for (a) vertical velocity (c.i. = 2 m s^{-1}) and (b) rainwater (c.i = 1 g kg^{-1}). Here the longitudinal positions are displayed in the ground-relative framework.

$$\frac{\Delta q_v}{\Delta t}=\frac{\Delta q_{vs}}{\Delta t}+E_r, \tag{20}$$

$$\frac{\Delta q_c}{\Delta t}=-\frac{\Delta q_{vs}}{\Delta t}-A_r-C_r, \tag{21}$$

$$\frac{\Delta q_r}{\Delta t}=-E_r+A_r+C_r-V_r\frac{dq_r}{dz}. \tag{22}$$

Here L is the latent heat of condensation, A_r is the autoconversion rate of cloud water to rainwater, C_R is the collection rate of rainwater, E_r is the rainwater evaporation rate, and V_r is the rainwater terminal velocity. For each variable ϕ, $\Delta\phi=\phi^{t+\Delta t}-\phi^*$, where ϕ^* is the value at the new time level prior to the final microphysics update.

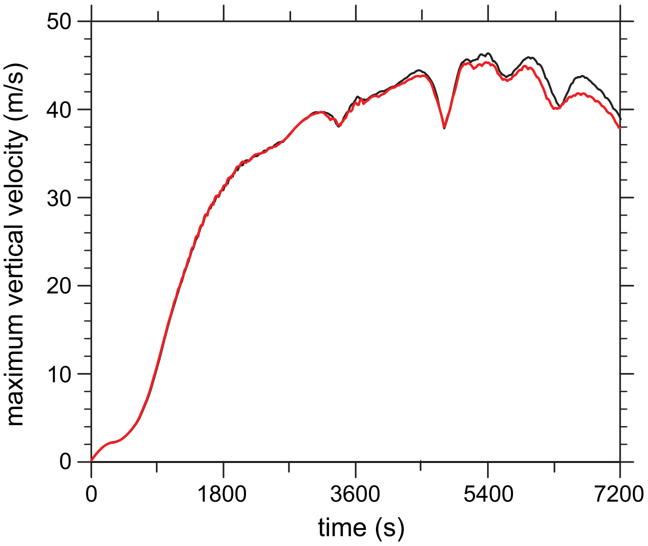

Figure 12. Maximum vertical velocity of the supercell updraft for simulations on a flat plane with $\Delta \sim 500$ m (red line) and on the reduced-radius sphere with $X = 120$ and $\Delta \sim 500$ m (black line).

3.5. Physical and Numerical Diffusion

As mentioned above, dissipation plays a strong role in regulating the intensity and structure of simulated supercell storms, and is an important component of convective storm simulations. For this test case, we have specified constant-coefficient ($\nu = 500$ m^2/s) second-order diffusion terms (both horizontal and vertical) in each of the prognostic equations, with an inverse Prandtl number of 3 for the scalar equations. In the vertical direction, this mixing is applied to the perturbation from the initial mean state to prevent the initial balanced state from being mixed out as the simulation progresses (this would not be needed in a more realistic subgrid turbulence scheme). Although this is not as realistic as a subgrid TKE or Smagorinski scheme, using a constant physical viscosity allows the numerical solutions to be converged as the grid is sufficiently refined (which will not occur using TKE or Smagorinsky because of their dependence on the grid scale). With this second-order diffusion, no additional explicit higher-order filters are included.

We have also experimented with using fourth-order horizontal filters instead of second-order diffusion terms. In these tests, we found that it was necessary to retain the second-order vertical diffusion as described above in order to avoid accumulating significant noise in the evolving fields. With the fourth-order horizontal filters, the storm system evolved somewhat more rapidly and exhibited more smaller-scale structure.

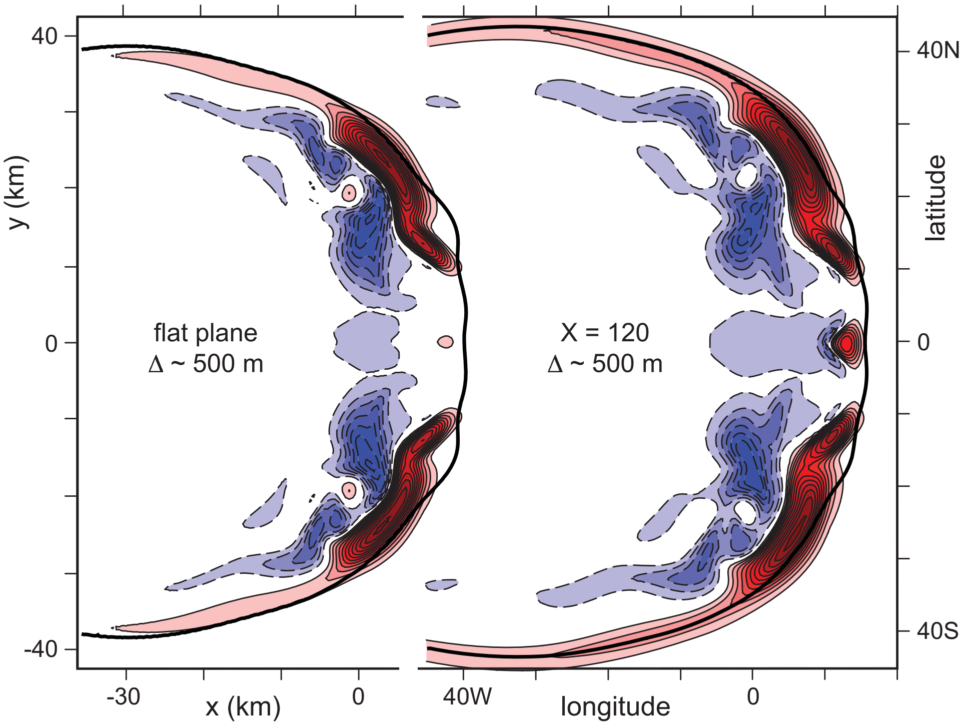

Figure 13. Horizontal cross sections at 2.5 km at 2 h of vertical velocity (c.i. = 1 ms^{-1}), displayed for simulations (left) on a flat plane with $\Delta \sim 500$ m and (right) on the reduced-radius sphere with $X = 120$ and $\Delta \sim 500$ m. The heavy solid line depicts the location of the leading edge of the surface cold pool.

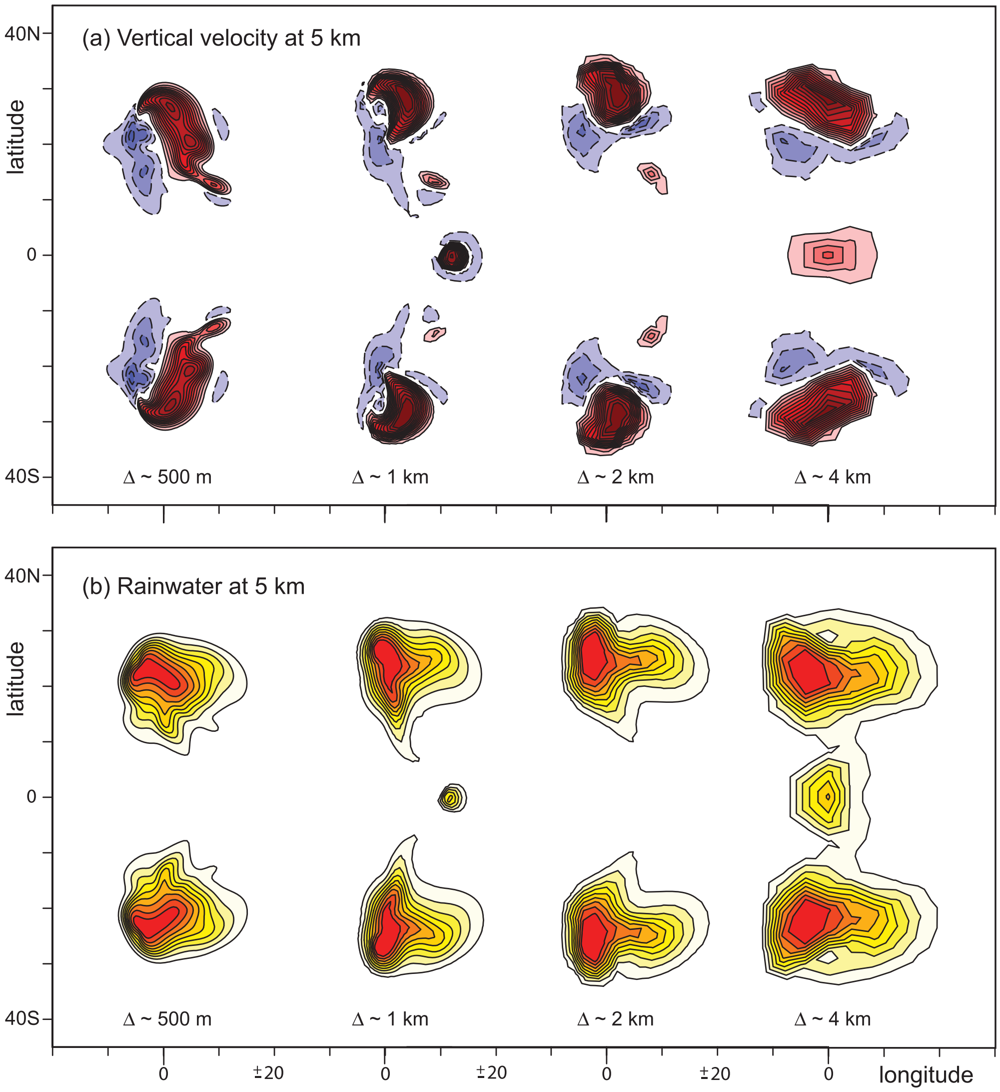

Figure 14. Horizontal cross sections at 5 km at 2 h of (a) vertical velocity (c.i. = 2 ms^{-1}), and (b) rainwater (c.i = 1 gm/kg). Fields are displayed for simulations on the reduced-radius sphere for horizontal grid spacings of $\Delta \sim 0.5$ km, $\Delta \sim 1.0$ km, $\Delta \sim 2.0$ km, and $\Delta \sim 4.0$ km (from left to right).

3.6. MPAS Results for Supercell Simulations

Simulations were integrated over a 2 h time interval, with convection initiated by the warm bubble described in section 3.3. The overall evolution of the splitting supercells is well illustrated by the horizontal cross sections of vertical velocity and rainwater at 5 km at half hour intervals shown in Figure 11. Here the longitudinal position of the fields are shown based on a ground relative framework (i.e., the $U_c = 15$ m s^{-1} has been added back into the translation speed of the storm). At 30 min, a single strong updraft is producing significant precipitation that is collocated with the updraft. By 1 h, the initial updraft has split into two distinct updraft cells due to the negative buoyancy associated with rainwater loading along the central line of symmetry (equator), together with favorable lifting vertical pressure gradients on the flanks of the rotating updrafts [*Rotunno and Klemp*, 1982, 1985]. By 90 min, the storm splitting has produced two mirror-image supercell storms, one with cyclonic updraft rotation propagating to the right (south) of the mean winds, and the other rotating anticyclonically and propagating to the left (north) of the mean winds. Owing to their transverse propagation, the two supercells continue to move farther apart over the second hour.

The physical relevance of the supercell simulation on an $X = 120$ reduced-radius sphere can be established through comparisons with a corresponding simulation in Cartesian geometry. For this purpose, we have configured an MPAS grid to represent a flat plane of hexagonal grid cells with periodic lateral boundary

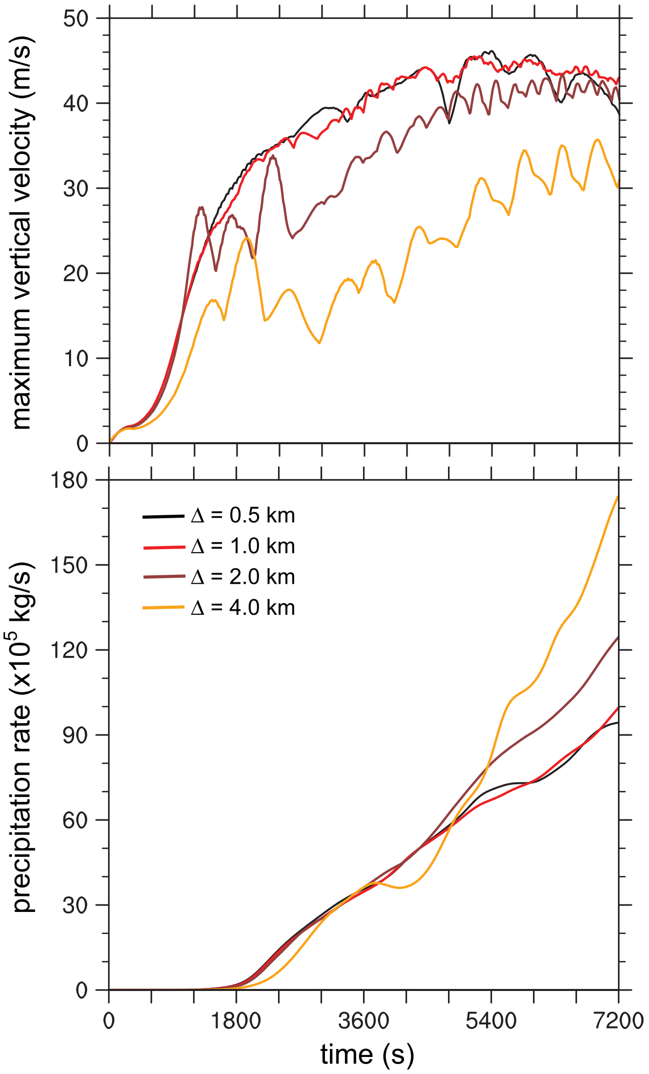

Figure 15. Time variation of the (a) maximum updraft vertical velocity and (b) precipitation rate for supercell simulations with sphere-radius reduction $X = 120$ for $\Delta \sim 0.5$ km (black line), $\Delta \sim 1.0$ km (red line), $\Delta \sim 2.0$ km (brown line), and $\Delta \sim 4.0$ km (yellow line).

conditions in the east-west and north-south directions. The horizontal domain dimensions are 168 × 168 km with a nominal cell spacing of 500 m. Figure 12 displays the time evolution of the maximum vertical velocity w_{max} in both the reduced-radius sphere and the flat-plane simulations. The rapid rise in w_{max} over the initial 40–50 min is associated with the growth of the initial convective cell. As this initial cell splits into two rotating supercells, w_{max} levels off and maintains an amplitude in the range 40–45 m s^{-1}. This comparison confirms that the reduced-radius sphere simulation exhibits good quantitative agreement with the simulation in a Cartesian plane. We note that the w_{max} profile shown here for the flat-plane simulation differs somewhat from the results presented by *Skamarock et al*. [2012] for a comparable supercell simulation with MPAS; after about 40 min, the w_{max} in the current simulation is slightly stronger. This difference arises because the *Skamarock et al*. [2012] simulation employed a horizontal domain (84 × 84) that was half the current size, and effects of the periodic lateral boundaries were influencing the results at later times. (*Skamarock et al*. [2012] also used a 30 m s^{-1} shear over 5 km, not 25 m s^{-1} as stated in that paper.)

Further comparison of the flat-plane and reduced-radius sphere simulations is provided in Figure 13, which displays the vertical velocity fields at $z = 2.5$ km at 2 h, along with the location of the leading edge of the surface cold pool (taken here as the $-0.3°$ perturbation potential temperature contour at the lowest model half level at $z = 250$ m). (Here the horizontal scales have been adjusted so the horizontal distances in km are the same.) At this 2.5 km level, the updrafts are clearly aligned above the convergence line that forms along the edge of the surface cold pool, and are quite similar in the two simulations. Notice, however, that in the $X = 120$ simulations the cold pool (and the lower level updrafts) extends laterally to slightly higher latitudes than in the flat-plane simulation. We believe that this small discrepancy is caused by the differing environmental conditions that the storms encounter as they propagate to higher latitudes. The speed at which the cold air spreads out beneath the storm is governed in part by the temperature difference across the leading edge of the pool (analogous to a gravity current). In the $X = 120$ simulations, the low-level environmental air is somewhat warmer at higher latitudes due to the gradient wind balance imposed on the initial environmental state (see Figure 10). Thus, the cold pool and its associated convergence line in the $X = 120$ simulations propagate laterally a little more rapidly with increasing latitude than in the simulation on a flat plane.

We have also conducted supercell simulations with horizontal grid spacings of $\Delta \sim 1$ km ($\sim$1.1° mesh containing 40,962 grid cells), 2 km ($\sim$2.2° mesh containing 10,242 grid cells), and 4 km ($\sim$4.3° mesh containing 2562 grid cells) to assess the impact of reduced horizontal grid resolution on the evolution and structure of the simulated suprecells. Figure 14 displays the vertical velocity and rainwater fields at 5 km at 2 h for the range of horizontal grid spacings from 0.5 to 4 km. Although noticeable quantitative differences are evident in the structures of these vertical velocity and rainwater fields, the overall structure and propagation of the splitting supercells is quite similar across this range of horizontal resolution. In the coarsest resolution $\Delta \sim 4$ km simulation, however, there is noticeably less detail in the convective structure and horizontal extent of the supercells is larger (particularly in the rainwater field). These results are consistent with those from previous studies that have found that the overall structure of convective systems could be reasonably captured in forecast simulations with explicit treatment of convection with horizontal grid spacings of about 4 km or less [*Weisman et al*., 1997, 2008; *Kain et al*., 2008].

The resolution dependence of the evolving supercells is further illustrated in Figure 15, depicting the time variation of the maximum vertical velocity and the overall precipitation rate over the 2 h integrations. The close quantitative agreement between the $\Delta \sim 0.5$ and 1.0 km results suggests that the macroproperties of the convection are nearly converged at these resolutions. As the horizontal grid spacing is further increased, the maximum updraft intensity decreases while the precipitation rate increases (over the second hour). This sensitivity is to be expected given the marginal resolution of the updraft cells at the coarser resolutions. The increased precipitation rate produced by the less intense updrafts appears to result from the increased horizontal extent of the rainwater fields in the underresolved simulations.

To assess the sensitivity of the supercell results to the time step, we reran the 2 km simulation (originally conducted with a 12 s time step) with a 6 and 3 s time step. The results with these smaller time steps are nearly indistinguishable from those at the larger time, confirming that the coarser time step is sufficient to represent the convective processes.

4. Summary

Evaluating the behavior of global models at nonhydrostatic scales can be a significant challenge since simulation with O(km) global grids required to resolve these scales are computationally of prohibitive expense. Within MPAS, this computational burden can be avoided by reconfiguring the unstructured global Voronoi mesh to correspond to a flat plane of hexagonal grid cells with doubly periodic lateral boundaries. This option, however, is typically not available in other nonhydrostatic global models, which limits the opportunities for intercomparing models in this configuration. Nonhydrostatic processes can be economically simulated in a global context if the radius of the sphere is significantly reduced. In our view, the magnitude of the sphere-radius reduction should be constrained such that the nonhydrostatic results on the smaller sphere maintain strong similarity to the corresponding results obtained in a Cartesian geometry. This correspondence confirms the physical realism of the simulated phenomena and permits quantitative comparisons with previously documented analytic and numerical solutions. The mountain-wave and supercell test cases presented above satisfy this requirement as the results from simulations on the reduced-radius sphere exhibit close correspondence with the results obtained in a Cartesian geometry.

Appendix A: Two-Dimensional Linear Analytic Solution for a Schär Mountain

The linear wave equation for flow with an isothermal mean state T_0 and a constant mean wind U is well suited for analysis, since it can be written in a form that has constant coefficients. Removing the dependency on the mean density profile

$$w(x,z)=\left(\frac{\rho_0}{\bar{\rho}}\right)^{\frac{1}{2}} w_1(x,z)=\exp\left(\frac{\beta z}{2}\right) w_1(x,z), \tag{A1}$$

w_1 is periodic with height and satisfies the wave equation:

$$\nabla^2 w_1+\left(\frac{N^2}{U^2}-\frac{\beta^2}{4}\right) w_1=0, \tag{A2}$$

where

$$N^2=\frac{g^2}{c_p T_0}, \quad \text{and} \quad \beta=\frac{g}{R_d T_0}. \tag{A3}$$

For a single Fourier mode, $w_1(x,z)=\hat{w}_1(k,z)\exp(ikx)$, and (A2) becomes:

$$\frac{d^2\hat{w}_1}{dz^2}+m^2\hat{w}_1=0, \tag{A4}$$

where

$$m^2=\frac{N^2}{U^2}-\frac{\beta^2}{4}-k^2. \tag{A5}$$

The lower boundary terrain profile is given by

$$h(x)=h_0\exp\left(-\frac{x^2}{d^2}\right)\cos^2\frac{\pi x}{\xi}, \tag{A6}$$

and its corresponding Fourier transform is

$$\hat{h}(k)=h_0\int_0^\infty \exp\left(-\frac{x^2}{d^2}\right)[1+\cos Kx]\cos kx\,dx, \tag{A7}$$

$$=\frac{\sqrt{\pi}}{4}h_0 d\left\{\exp\left[-\frac{d^2}{4}(K+k)^2\right]+2\exp\left[-\frac{d^2}{4}k^2\right]+\exp\left[-\frac{d^2}{4}(K-k)^2\right]\right\}, \tag{A8}$$

where $K=2\pi/\xi$. Solving (A4) subject to the lower boundary condition $\hat{w}_1(k,0)=ikU\hat{h}(k)$ and applying a radiation condition to ensure upward propagation of wave energy, yields:

$$\hat{w}_1(k,z)=ikU\hat{h}(k)\left\{\begin{array}{lll}\exp[i\,\mathrm{sgn}(k)mz] & \text{for} & m^2>0\\ \exp(-|m|z) & \text{for} & m^2<0\end{array}\right\}. \tag{A9}$$

Taking the inverse Fourier transform recovers the 2-D vertical velocity field,

$$\begin{aligned}w(x,z)&=\frac{1}{2\pi}\exp\left(\frac{\beta z}{2}\right)\int_{-\infty}^{\infty}\hat{w}_1(k,z)\exp(ikx)\,dk\\ &=-\frac{U}{\pi}\exp\left(\frac{\beta z}{2}\right)\left\{\int_0^{k^*}k\,\hat{h}(k)\sin(mz+kx)\,dk+\int_{k^*}^{\infty}k\,\hat{h}(k)\exp(-|m|\,z)\sin kx\,dk\right\},\end{aligned} \tag{A10}$$

where

$$k^*=\left(\frac{N^2}{U^2}-\frac{\beta^2}{4}\right)^{\frac{1}{2}}. \tag{A11}$$

Appendix B: Three-Dimensional Linear Analytic Solution for a Circular Mountain

The 3-D linear wave equation for flow with an isothermal mean state T_0 and a constant mean wind U can be derived in the same manner as the 2-D wave equation in Appendix A. For a single horizontal Fourier mode, $w_1(x,y,z)=\hat{w}_1(k,l,z)\exp[i(kx+ly)]$, the 3-D counterparts to (A4) and (A5) become:

$$\frac{d^2\hat{w}_1}{dz^2}+m^2\hat{w}_1=0, \tag{B1}$$

with

$$m^2=\frac{k^2+l^2}{k^2}\left(\frac{N^2}{U^2}-k^2\right)-\frac{\beta^2}{4}. \tag{B2}$$

The circular terrain profile is given by

$$h(x)=h_0\exp\left(-\frac{x^2+y^2}{d^2}\right)\cos^2\left(\frac{\pi}{\xi}\sqrt{x^2+y^2}\right), \tag{B3}$$

and its corresponding Fourier transform is

$$\hat{h}(k,l)=4h_0\int_0^\infty\int_0^\infty \exp\left(-\frac{x^2+y^2}{d^2}\right)\cos^2\left(\frac{\pi}{\xi}\sqrt{x^2+y^2}\right)\cos kx\cos ly\, dy\, dx. \tag{B4}$$

Solving (B1) subject to the lower boundary condition $\hat{w}_1(k,l,0)=ikU\hat{h}(k,l)$ and applying a radiation condition to ensure upward propagation of wave energy, yields:

$$\hat{w}_1(k,l,z)=ikU\hat{h}\left(k,l\right)\left\{\begin{array}{ll}\exp\left[i\,\mathrm{sgn}(k)mz\right] & \text{for} \quad m^2>0\\ \exp\left[-|m|z\right] & \text{for} \quad m^2<0\end{array}\right\}. \tag{B5}$$

The 3-D vertical velocity field is then obtained by taking the inverse Fourier transform of (B5):

$$\begin{aligned} w(x,y,z)&=\frac{1}{4\pi^2}\exp\left(\frac{\beta z}{2}\right)\int_{-\infty}^{\infty}\int_{-\infty}^{\infty}\hat{w}_1(k,l,z)\exp\left[i(kx+ly)\right]\,dkdl\\ &=-\frac{U}{\pi^2}\exp\left(\frac{\beta z}{2}\right)\int_0^\infty\left\{\int_0^{k^*}k\,\hat{h}(k,l)\sin\left(mz+kx\right)dk+\int_{k^*}^{\infty}k\,\hat{h}(k,l)\exp\left[-|m|\,z\right]\sin kx\,dk\right\}\cos ly\,dl, \end{aligned} \tag{B6}$$

where k^* is the value of k for which $m=0$ in (B2). To evaluate this linear solution, the forward transform of the terrain (B4) and the inverse transform to recover w in (B6) are integrated numerically.

Appendix C: Listing of the Kesler Microphysics Subroutine

```
!-----------------------------------------------------------------------
      subroutine KESSLER( t, qv, qc, qr, rho, pk, dt, z, nz, rainnc )
!-----------------------------------------------------------------------
!
!     The KESSLER subroutine implements the Kessler (1969) microphysics
!     parameterization as described by Soong and Ogura (1973) and Klemp
!     and Wilhelmson (1978, KW). KESSLER is called at the end of each
!     time step and makes the final adjustments to the potential
!     temperature and moisture variables due to microphysical processes
!     occurring during that time step. KESSLER is called once for each
!     vertical column of grid cells. Increments are computed and added
!     into the respective variables. The Kessler scheme contains three
!     moisture categories: water vapor, cloud water (liquid water that
!     moves with the flow), and rain water (liquid water that falls
!     relative to the surrounding air). There  are no ice categories.
!     Variables in the column are ordered from the surface to the top.
!------------------------- input variables -----------------------------
!     t      - potential temperature (K)
!     qv     - water vapor mixing ratio (g/g)
!     qc     - cloud water mixing ratio (g/g)
!     qr     - rain  water mixing ratio (g/g)
!     rho    - dry air density (not mean state as in KW) (kg/m^3)
!     pk     - Exner function  (not mean state as in KW) (p/p0)**(R/cp)
!     dt     - time step (s)
!     z      - heights of thermodynamic levels in the grid column (m)
!     nz     - number of thermodynamic levels in the column
!     rainnc - accumulated precip beneath the grid column (mm)
!------------------------ output variables -----------------------------
!     Increments are added into t, qv, qc, qr, and rainnc which are
!     returned to the routine from which KESSLER was called. To obtain
!     the total precip qt, after calling the KESSLER routine, compute:
!       qt = sum over surface grid cells of (rainnc * cell area)  (kg)
!       [here, the conversion to kg uses (10^3 kg/m^3)*(10^-3 m/mm) = 1]
!-----------------------------------------------------------------------
      implicit none
      real t (nz), qv   (nz), qc   (nz), qr (nz), rho(nz), z (nz)
      real r (nz), rhalf(nz), velqr(nz), sed(nz), pk (nz), pc(nz)
      real rd, cp, lv, ern, qrprod, prod, qvs, psl, dt, rhoqr, rainnc
      integer k, nz
```

```
!---------------------- physical constants ------------------------------------
      rd     = 287.        !  gas constant for dry air, J/(kgK)
      cp     = 1003.       !  heat capacity at constant pressure, J/(kgK)
      lv     = 2.5e6       !  latent heat of vaporization, J/kg
      psl    = 1000.       !  reference sea level pressure, mb
      rhoqr  = 1000.       !  density of liquid water, kg/m^3
!------------------------------------------------------------------------------
      do k=1,nz
         r(k)     = 0.001*rho(k)
         rhalf(k) = sqrt(rho(1)/rho(k))
!------- liquid water terminal velocity (m/s) following KW eq. 2.15
         velqr(k)  = 36.34*(qr(k)*r(k))**0.1364*rhalf(k)
      end do
```

```
!---- precipitation accumulated beneath the column
      rainnc = rainnc + 1000.*rho(1)*qr(1)*velqr(1)*dt/rhoqr    ! mm rain
!---- sedimentatiion term using upstream differencing
      do k=1,nz-1
         sed(k) = dt*(r(k+1)*qr(k+1)*velqr(k+1)                         &
                     -r(k  )*qr(k  )*velqr(k  ))/(r(k)*(z(k+1)-z(k)))
      end do
      sed(nz)  = -dt*qr(nz)*velqr(nz)/(.5*(z(nz)-z(nz-1)))
      do k=1,nz
!------- autoconversion and accretion rates following KW eq. 2.13a,b
         qrprod = qc(k) - (qc(k)-dt*amax1(.001*(qc(k)-.001), 0.))        &
                                    /(1.+dt*2.2*qr(k)**.875)
         qc(k) = amax1(qc(k)-qrprod,0.)
         qr(k) = amax1(qr(k)+qrprod+sed(k),0.)
!------- saturation vapor mixing ratio (g/g) following KW eq. 2.11
         pc(k) = 3.8/(pk(k)**(cp/rd)*psl)
         qvs   = pc(k)*exp(17.27*(pk(k)*t(k)-273.)                     &
                                /(pk(k)*t(k)- 36.))
!------- water vapor adjustment to reach saturation following KW eq. 3.9
         prod  = (qv(k)-qvs)/(1.+qvs*(4093.*lv/cp)/(pk(k)*t(k)-36.)**2)
!------- evaporation following KW eq. 2.14a,b
         ern   = amin1(dt*(((1.6+124.9*(r(k)*qr(k))**.2046)             &
                    *(r(k)*qr(k))**.525)/(2.55e6*pc(k)                  &
                    /(3.8 *qvs)+5.4e5))*(dim(qvs,qv(k))                 &
                    /(r(k)*qvs)),amax1(-prod-qc(k),0.),qr(k))
!------- saturation adjustment following KW eq. 3.10
         t (k) = t(k) + lv/(cp*pk(k))*(amax1( prod,-qc(k))-ern)
         qv(k) = amax1(qv(k)-max(prod,-qc(k))+ern,0.)
         qc(k) = qc(k)+max(prod,-qc(k))
         qr(k) = qr(k)-ern
      end do
      end subroutine KESSLER
!-------------------------------------------------------------------------
```

References

Ching, J., R. Rotunno, M. LeMone, A. Martilli, B. Kosovic, P. A. Jimenez, and J. Dudhia (2014), Convectively induced secondary circulations in fine-grid mesoscale numerical weather prediction models, *Mon. Weather Rev.*, *142*, 3284–3302.

Gal-Chen, T., and R. C. J. Sommerville (1975), Numerical solutions of the Navier-Stokes equations with topography, *J. Comput. Phys.*, *17*, 276–310.

Kain, J. S., et al. (2008), Some practical considerations regarding horizontal resolution in the first generation of operational convection-allowing NWP, *Weather Forecast.*, *23*, 931–952.

Kessler, E. (1969), *On the Distribution and Continuity of Water Substance in Atmospheric Circulation, Meteorol. Monogr.*, vol. 32, 84 pp., Am. Meteorol. Soc., Boston, Mass.

Klemp, J. B., and R. B. Wilhelmson (1978), The simulation of three-dimensional convective storm dynamics, *J. Atmos. Sci.*, *35*, 1070–1096.

Klemp, J. B., W. Skamarock, and O. Fuhrer (2003), Numerical consistency of metric terms in terrain-following coordinates, *Mon. Weather Rev.*, *131*, 1229–1239.

Klemp, J. B., J. Dudhia, and A. D. Hassiotis (2008), An upper gravity-wave absorbing layer for NWP applications, *Mon. Weather Rev.*, *136*, 3987–4004.

Malardel, S. (2013), Physics/dynamics coupling at very high resolution: Permitted versus parametrized convection, in *ECMWF Seminar on Recent Developments in Numerical Methods for Atmosphere and Ocean Modelling*, pp. 83–98, ECMWF, Reading, U. K. [Available at http://old.ecmwf.int/publications/library/ecpublications/_pdf/seminar/2013/Malardel.pdf.]

Rayleigh, L. (1916), LIX. On convection currents in a horizontal layer of fluid, when the higher temperature is on the under side, *Philos. Mag.*, *32*, 529–546.

Rotunno, R., and J. B. Klemp (1982), The influence of the shear-induced pressure gradient on thunderstorm motion, *Mon. Weather Rev.*, *110*, 136–151.

Rotunno, R., and J. B. Klemp (1985), On the rotation and propagation of simulated supercell thunderstorms, *J. Atmos. Sci.*, *42*, 271–292.

Schär, C., D. Leuenberger, O. Fuhrer, D. Lüthi, and C. Girard (2002), A new terrain-following vertical coordinate formulation for atmospheric prediction models, *Mon. Weather Rev.*, *130*, 2459–2480.

Schlesinger, R. E. (1975), A three-dimensional numerical model of an isolated deep convective cloud: Preliminary results, *J. Atmos. Sci.*, *32*, 934–957.

Schlesinger, R. E. (1980), A three-dimensional numerical model of an isolated thunderstorm. Part II: Dynamics of updraft splitting and mesovortex couplet evolution, *J. Atmos. Sci.*, *37*, 395–420.

Skamarock, W. C., and A. Gassmann (2011), Conservative transport schemes for spherical geodesic grids: High-order flux operators for ODE-based time integration, *Mon. Weather Rev.*, *139*, 2962–2975.

Skamarock, W. C., J. B. Klemp, M. G. Duda, L. Fowler, S.-H. Park, and T. D. Ringler (2012), A Multi-scale nonhydrostatic atmospheric model using centroidal Voronoi tesselations and C-grid staggering, *Mon. Weather Rev.*, *240*, 3090–3105.

Soong, S.-T., and Y. Ogura (1973), A comparison between axisymmetric and slab-symmetric cumulus cloud models, *J. Atmos. Sci.*, *30*, 879–893.

Ullrich, P. A., C. Jablonowski, J. Kent, P. H. Lauritzen, R. D. Nair, and M. A. Taylor (2012), *Dynamical Core Model Intercomparison Project (DCMIP) Test Case Document*, Earth System CoG. [Available at www.earthsystemcog.org.]

Wedi, P. W., and P. K. Smolarkiewicz (2009), A framework for testing global non-hydrostatic models, *Q. J. R. Meteorol. Soc.*, *35*, 46–484.

Weisman, M. L., and J. B. Klemp (1982), The dependence of numerically simulated convective storms on vertical wind shear and buoyancy, *Mon. Weather Rev.*, *110*, 504–520.

Weisman, M. L., and J. B. Klemp (1984), The structure and classification of numerically simulated convective storms in directionally varying wind shears, *Mon. Weather Rev.*, *112*, 2479–2498.

Weisman, M. L., and J. B. Klemp (1986), Characteristics of isolated convective storms, in *Mesoscale Meteorology and Forecasting*, pp. 331–358, Am. Meteorol. Soc., Boston, Mass.

Weisman, M. L., J. B. Klemp, and R. Rotunno (1988), The structure and evolution of numerically simulated squall lines, *J. Atmos. Sci.*, *45*, 1990–2013.

Weisman, M. L., W. C. Skamarock, and J. B. Klemp (1997), The resolution dependence of explicitly modeled convective systems, *Mon. Weather Rev.*, *125*, 527–548.

Weisman, M. L., C. Davis, W. Wang, K. W. Manning, and J. B. Klemp (2008), Experiences with 0–36-h explicit convective forecasts with the WRF-ARW Model, *Weather Forecas.*, *23*, 407–437.

Wilhelmson, R. (1974), The life cycle of a thunderstorm in three dimensions, *J. Atmos. Sci.*, *31*, 1629–1651.